Green Chemistry

PAPER

View Article Online
View Journal | View Issue

Cite this: *Green Chem.*, 2015, **17**, 2164

Plasma-enabled sustainable elemental lifecycles: honeycomb-derived graphenes for next-generation biosensors and supercapacitors†

Dong Han Seo,‡[a,b] Shafique Pineda,‡[a,b] Samuel Yick,[a,b] John Bell,[c] Zhao Jun Han[a] and Kostya (Ken) Ostrikov*[a,b,c]

Received 3rd November 2014,
Accepted 10th December 2014

DOI: 10.1039/c4gc02135e

www.rsc.org/greenchem

A green and efficient conversion of redundant biomass into functional nanomaterials holds the key to sustainable future technologies. Recently, vertical graphene nanosheets (VGS) have emerged as promising nanomaterials for integration in high-performance biosensors and supercapacitors, owing to their excellent and unique structural, morphological and electrical properties. However, when considering the conventional techniques utilized in nanofabrication, such as thermal or chemical routes, these often involve complex, eco-destructive and resource-consuming processes. Here we report on a single-step, potentially scalable, environmentally-benign and plasma-enabled method to synthesize VGS from an underutilized and natural by-product precursor, honeycomb. The VGS multifunctionality is highlighted by its integration as supercapacitor electrodes for energy storage, and as an electrochemical biosensor for the detection of the neurotoxic Amyloid-beta (Aβ) biomarker of Alzheimer's disease. The VGS were employed as binder-free supercapacitor electrodes, and demonstrated high specific capacitance up to 240 F g^{-1} at a scan rate of 5 mV s^{-1} and 100% capacitance retention after 2000 charge/discharge cycles. Furthermore, the VGS were functionalized with curcumin bioreceptors, and exhibited good sensitivity and selectivity towards the detection of neurotoxic Aβ species, and demonstrated a detection limit of 0.1 μg mL^{-1}.

Introduction

The rationale for implementing green technologies as part of a sustainable modern society is becoming increasingly apparent.[1] In particular, recycling redundant biomass into functional nanomaterials has attracted significant attention, notably, as this promotes a more efficient route for nanomaterial fabrication, as compared to conventional methods which utilize hazardous chemicals or purified hydrocarbon gases.[2,3] Moreover, an efficient synthesis of nanomaterials remains crucial for the large-scale commercialization of high-performance energy storage and biomedical devices. However, existing techniques for the transformation of biomass into nanostructures *via* thermal or chemical routes are not only precursor-specific, but are also often expensive, complex, as well as energy-, time- and resource-consuming.[4] Therefore, there is a need for a process to convert these chemically heterogeneous biomasses into uniform and useful functional nanostructures. Amongst a variety of nanomaterials, carbon-based nanostructures such as graphene have attracted significant interest owing to its exceptional opto-electrical and mechanical properties,[5] which are determined by its specific morphology, orientation and stacking order.[6,7]

Recently, vertical graphene nanosheets (VGS) emerged as a highly-promising nanomaterial for diverse applications such as supercapacitors and biosensors.[8] VGS possess a unique morphology of few-layered graphene sheets self-organized in an open 3D-inter-networked array structure.[9,10] Such morphological features enable the properties of a high surface area and good electrical conductivity, which are particularly important for the realization of high-performance supercapcitors and biosensors. Moreover, the presence of dense and thin reactive edge planes in VGS enhances its chemical and electrochemical activity.[8] Indeed, these reactive sites on VGS may

[a]*Plasma Nanoscience Laboratories, Industrial Innovation Program, Manufacturing Flagship, CSIRO, P.O. Box 218, Lindfield, NSW 2070, Australia. E-mail: Kostya.Ostrikov@csiro.au*
[b]*School of Physics, The University of Sydney, Sydney, NSW 2006, Australia*
[c]*Institute for Future Environments and Institute for Health and Biomedical Innovation, School of Chemistry, Physics, and Mechanical Engineering, Queensland University of Technology, Brisbane, QLD 4000, Australia*

†Electronic supplementary information (ESI) available: S1. Typical cross-sectional SEM image of HC-VGS with a height of ~2 μm. S2. Specific capacitance of VGS calculated from the charge/discharge curves. S3. EIS measurement for pristine HC-VGS. S4. Electrochemical performance of HC-VGS in a three-electrode cell configuration. S5. CV characterization for the attachment of curcumin onto HC-VGS. See DOI: 10.1039/c4gc02135e

‡These authors contributed equally to this work.

facilitate the immobilization of biological species, and thus, make VGS a promising base material for biosensing applications. Furthermore, while the open structure of VGS facilitates the transport of ions, its structural rigidity enhances the stability of ion storage capacitors, and thus, promotes the integration of VGS in energy storage devices.

Previous investigations have demonstrated the vital role of low-temperature plasmas for the deterministic fabrication of VGS.[11–13] In particular, such VGS structures can be formed using natural precursors in different heterogeneous chemical states by unique plasma-based processes that adhere to the basic principles of sustainability and green chemistry.[2,14,15] In particular, plasma not only enables the breakdown of chemically heterogeneous natural precursors into simpler building units of graphene, it also enables the self-organization of these building units into uniform VGS structures.[15] Therefore, plasma-based techniques present a promising approach for the effective conversion of diverse forms of biomass into functional nanomaterials. A particularly viable biomass is honeycomb. Typically after honey extraction, honeycomb is deemed to be redundant. As such, the remaining honeycomb is either disposed of, or recycled as a source of candle wax, or as an additive in cosmetics. Thus far, recycling of used honeycomb is primitive and limited. However, in this work, we utilized honeycomb, a natural wax composed of long-chain hydrocarbons, as a source for the fabrication of VGS.

Here, we demonstrate a single step, low-temperature, catalyst-free and highly efficient plasma-enabled reforming of the underutilized by-product honeycomb, into uniform VGS. Moreover, to demonstrate the multifunctionality of the honeycomb-derived vertical graphene nanosheets (HC-VGS), we directly integrated it as a supercapacitor electrode, which exhibited good electrochemical performance and stability. Furthermore, we demonstrate the functionality of HC-VGS as base material for the firm immobilization of curcumin, which in turn, enables the selective and sensitive detection of the neurotoxic Aβ biomarker of Alzheimer's disease.

Experimental methods

Plasma enabled growth of HC-VGS

The deposition of HC-VGS was carried out in a RF inductively coupled plasma CVD system. Flexible graphite paper and Ni foam was used as growth substrates for HC-VGS. The size of growth substrates was 6×1 cm^2. In order to provide a uniform coating of honeycomb on graphite paper, the honeycomb was first melted by heating at 100 °C. Subsequently, the substrates were coated evenly with the liquefied honeycomb, prior to being loaded in the reactor. A gas mixture of 10 sccm Ar and 10 sccm H_2 was fed into the chamber, then the plasma was generated at 2.0 Pa pressure and 1000 W RF power. Although no external substrate heating was used, during the 9 min deposition process the substrate temperature reached 400 °C due to the plasma-heating effects.

Microscopy and microanalysis

Field-emission scanning electron microscopic (FE-SEM) images were obtained by Zeiss Auriga microscope operated at 5 keV electron beam energy with an InLens secondary electron detector. Raman spectroscopy was performed using a Renishaw inVia spectrometer with a laser excitation at 514 nm (Ar laser) and a probing spot size of ~1 μm^2. X-ray photoelectron spectroscopy (XPS) spectra were recorded by Specs SAGE 150 spectroscope with the Mg Kα excitation at 1253.6 eV. Both survey and narrow scans of C 1s were conducted. The mass of the electrode was determined by weighting a 10 cm long sample on an ultrasensitive balance (Δ ± 0.1 μg; Mettler Toledo UMT2) and calculating the fractional mass which was submerged into the electrolyte.

Supercapacitor measurements

The electrochemical measurements were performed in 1 M Na_2SO_4 at room temperature. Both three-electrode and two-electrode cell configurations were employed. The three-electrode cell used the as-grown HC-VGS sample as the working electrode, a Pt foil as the counter electrode, and an Ag/AgCl reference electrode; while the two-electrode cell used two identical testing samples as the electrodes. Cyclic voltammetry (CV), galvanostatic charge/discharge, and electrochemical impedance spectroscopy (EIS) measurements were conducted using a BioLogic VSP 300 potentiostat/galvanostat device. CV tests were performed in the potential range of 0–1 V at scan rates of 5–500 mV s^{-1}. Galvanostatic charge/discharge curves were obtained at a constant current density of 3, 2, and 1 mA cm^{-2}. EIS measurements were performed in the frequency range from 0.01 Hz to 100 kHz. The specific capacitance of single electrode C_s was calculated from the CV curves in two electrode measurement by integrating the discharge current against the potential V according to $C_s = (2\int I\mathrm{d}V/vm\Delta V)$, where v is the scan rate (V s^{-1}), m is the mass of the active material in single electrode, and ΔV is the operating potential window (1 V). Similarly, specific capacitance was calculated from the charge/discharge curve according to $C_s = 2I/(m\mathrm{d}V/\mathrm{d}t)$, where I is the discharging current, m is the mass of active material, dV potential window (1 V) and dt is the discharge time. The surface mass density of active material was 0.4 mg cm^{-2} and 1×1 cm^2 of the sample was used as the working electrode in the test.

Biosensing measurements

The electrochemical measurements were conducted in 20 mM phosphate buffer with 0.15 M NaCl at room temperature. A three-electrode cell configuration was employed. The three-electrode cell used the as-grown HC-VGS sample (size of 1×0.5 cm^2) as the working electrode, a Pt foil as the counter electrode, and an Ag/AgCl reference electrode.

Curcumin, from *curcuma longa* (Sigma Aldrich), was dissolved to 2% w/v in DMSO and drop-cast onto HC-VGS, and left to dry overnight at room temperature and pressure. Monomeric and oligomeric Amyloid-beta 42 (Aβ) were prepared

according the protocol outlined by Youmans *et al.* (Biosensis).[16] Briefly, 45 μg of lyophilized Aβ peptide was reconstituted with 2 μL of DMSO, and 98 μL of F12 K medium was added to give a total Aβ peptide concentration of 450 μg mL^{-1}. Monomeric Aβ (Aβ-M) was taken at this point, whereas oligomers (Aβ-O) were formed by incubating the solution for 24 hours at 4 °C. The curcumin functionalized HC-VGS was subjected to successive incubations with Aβ-M or Aβ-O (at concentrations of 10, 1 and 0.1 μg mL^{-1}) for 20 minutes at room temperature and pressure for each concentration. Subsequently, EIS measurements were conducted in the frequency range from 1 Hz to 5 MHz using a BioLogic VSP 300 potentiostat/galvanostat device. The R_{ct} (charge-transfer resistance) of the sensor following incubation with Aβ was expressed as a percentage of the R_{ct} in the reference case, which was incubated in DMSO/F12 K medium in the absence of Aβ.

Results and discussion

Fabrication and structure of HC-VGS

Flexible and light-weight energy storage and medical devices play a central role in the future development of multifunctional electronics such as portable and wearable devices, roll-up displays, and photovoltaic cells.[17] To this end, flexible graphite paper and Ni foam were chosen as the growth substrates for HC-VGS. Due to its good electrical conductivity, Ni foam and graphite paper also functions as the current collectors in the supercapacitor and biosensing electrodes.

The procedure for preparing HC-VGS is illustrated in Fig. 1(a). In particular, HC-VGS was formed through the unique plasma transformation of a natural by-product precursor, honeycomb. This approach features a cheap, low-temperature, and environmentally-benign alternative to the chemical vapor deposition (CVD) processes which involve highly explosive hydrocarbon precursor gases such as CH_4 and C_2H_2.[2,3]

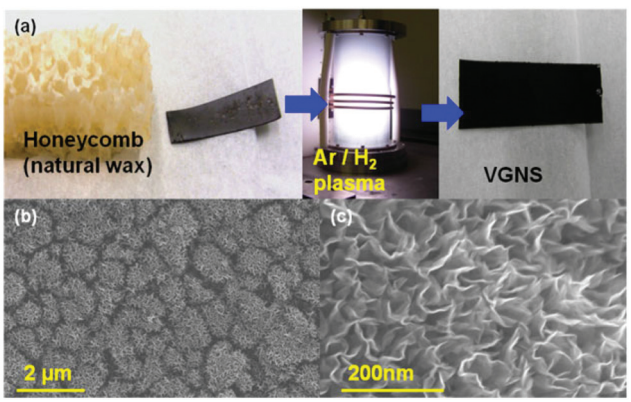

Fig. 1 Transformation of honeycomb (natural wax) into vertical graphenes in a reactive Ar + H_2 plasma-based process. (a) Honeycomb was liquefied on the graphite paper substrate which was placed in an ICP-CVD system, whereupon a short plasma exposure was utilized to reform the honeycomb precursor and grow the HC-VGS. As-grown HC-VGS on flexible graphite substrate with supporting (b) SEM; and (c) high-resolution SEM images featuring its morphology.

The used natural by-product precursor, honeycomb, consisted of mostly palmitate, palmitoleate, and oleate esters of long-chain aliphatic alcohols. Honeycomb is typically solid at room temperature, and can be easily liquefied and coated on the substrates. During the early growth process (~2 min), the long chain of carbon groups in honeycomb were broken down into carbon building units owing to the rapid plasma dissociation of the material. Subsequently, these carbon building units were re-formed into hexagonal carbon-rings, which are the basic elements for the construction of graphene nanosheets. Such plasma-unique effects were presumably attributed to the strong plasma-matter interactions in the plasma sheath.[18] In particular, H_2 can enhance the surface flux of these building units through the recombination-mediated energy dissipation on the surface and facilitate the nucleation and growth of VGS.[14] Moreover, the electric field in the plasma sheath also guides the vertical growth of graphene nanosheets.

Fig. 1(b) and (c) show the scanning electron microscopy (SEM) images of HC-VGS obtained after the direct growth process. An inherently open, 3D network with dense and uniform graphene nanosheets was clearly observed to cover the entire surface of graphite paper (see Fig. 1(a)). It is known that the morphology of VGS can be controlled during the plasma-enabled growth. Plasma parameters such as RF power, processing time, and gas composition affect the growth environment which will impact the morphology and structure of VGS. In our case, these graphene nanosheets were highly porous and exhibited an average sheet length of 200 nm and a typical thickness of 2 μm (Fig. 1c and S1†). This open structure may facilitate the access of biological targets and electrolyte ions to the active surfaces. Consequently, the morphology of HC-VGS not only provides a large surface area which is important for efficient charge transport in electrochemical capacitors. In addition, the evident high density of reactive edges may also promote a facile surface-immobilization of biological analytes.[18–20]

The surface chemical information of HC-VGS was also characterized by Raman and X-ray photoelectron spectroscopy (XPS). Fig. 2(a) illustrates the Raman spectra of HC-VGS. Three distinct peaks were present, namely, the characteristic disorder peak (D-band) at 1350 cm^{-1}, the graphitic peak (G-band) at 1580 cm^{-1}, and the second-order 2D-band at 2690 cm^{-1}. The G-band arises from the in-plane vibrational E_{2g} mode of the sp^2-hybridized carbon, the D-band is attributed to the finite crystallite size effect and various defects induced in the sp^2 carbon materials, and the 2D-band is a second-order Raman spectral feature due to the three-dimensional interplanar stacking of hexagonal carbon networks.[21–24] The ratios of Raman $I_{2D}/I_G \sim (0.45)$ and $I_D/I_G \sim (0.72)$ indicate the presence of sharp edge planes and a dominant sp^2 graphitic structure in HC-VGS.[24,25]

Fig. 2(b) shows the XPS measurements of HC-VGS nanostructures. A single strong C 1s peak positioned at binding energy (BE) of ~284.5 eV was evident, implying the HC-VGS was comprised of mostly carbon atoms. Fig. 2(c)

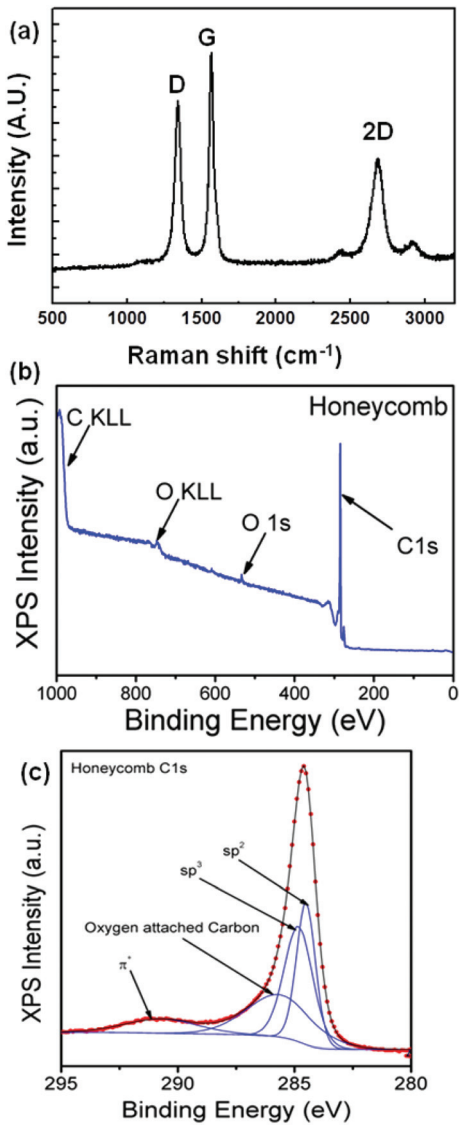

Fig. 2 (a) Raman spectrum of HC-VGS. (b) XPS survey scan and (c) C 1s narrow scan of HC-VGS. Spectrum was fitted with the sp^2, sp^3, oxygen-attached carbon, and $\pi-\pi^*$ shake-up features.

illustrates the C 1s narrow scan for HC-VGS. The C 1s spectra could be fitted by four peaks corresponding to the carbon sp^2 (BE ~ 284.5 eV), sp^3 (BE ~ 285.4 eV), carbon–oxygen bond (BE ~ 286 eV), and the energy loss "shake-up" feature (BE ~ 290.2 eV).[14,18] The sp^2 graphitic structure of HC-VGS also plays a major role in enhancing their charge storage capacity. Indeed, sp^2-bonded carbon is preferred over sp^3-bonded carbon in graphene-based supercapacitor electrodes, as the latter increases the charge transfer resistance and impedes the ability for charge storage. In particular, as HC-VGS features a large fraction of sp^2-hybridized carbon, in conjunction with a high C/O atomic ratio, this makes HC-VGS a highly desirable nanostructure for the integration in electrochemical energy storage devices.

Supercapacitor performance of HC-VGS electrodes

When considering widely available energy sources such as solar and wind power, their intermittent nature necessitates robust energy storage devices for these sources to be utilized in a commercial scale.[26] In addition, the needs for more capable energy storage devices are further stimulated by the recent advancements in portable electronics and hybrid electric vehicles.[27–29] Thus, supercapacitors which possess high power density, rapid charge/discharge rate, and a long lifespan are a particularly attractive option.[30–33]

The electrochemical performance of HC-VGS as binder-free supercapacitor electrodes was investigated by potentiostat/galvanostat measurements using the two-electrode configuration. Fig. 3(a) shows the cyclic voltammetry (CV) curves of HC-VGS in 1 M Na_2SO_4 aqueous electrolyte. Notably, the as-grown HC-VGS electrodes showed a nearly rectangular shape in CVs even at high scan rates (*e.g.*, 500 mV s^{-1}), suggesting the efficient formation of the electric double layer (EDL) and fast ion transport in the HC-VGS structure.[19] Fig. 3(b) shows the galvanostatic charge/discharge curves for HC-VGS at different current densities of 3, 2, and 1 mA cm^{-2}, respectively. A linear dependence between the discharge potential and time was identified in the discharge curves, further indicating the absence of major Faradaic processes.[34] These results are consistent with the structural analyses that the electrodes were composed of mostly carbon-based materials and the charge storage occurred mainly through the EDL mechanism.[35]

The specific capacitance *C* calculated from the CV curves at different scan rates is shown in Fig. 3(c). A decrease in the specific capacitance was observed as the scan rate was increased, similar to that of the corrugated 3D graphene sheets obtained by reduced graphene oxide.[36] It is also noted that HC-VGS exhibits a high specific capacitance of 240 F g^{-1} at 5 mV s^{-1} and 128 F g^{-1} at 2.5 A g^{-1} (Fig. S2†). We attributed such high specific capacitance to the large surface area, high electrical conductivity, and high electrochemical activity of the HC-VGS, which enables a facile access of ions to the edge and basal planes of the nanostructure.[31,37,38] This value of specific capacitance for HC-VGS structure is among the highest values reported for graphene based supercapacitor electrodes, and is also superior as compared to other carbon structures with a similar 3D morphology, such as the reduced graphene oxide sheets and the mechanically combined graphene/CNT hybrid structures.[39,40]

The cycle stability tests are shown in Fig. 3(d), in which HC-VGS exhibited 100% retention of its initial capacitance after 2000 cycles performed at a scan rate of 400 mV s^{-1}. In addition, the inset of Fig. 3(d) shows almost equivalent CV curves between the 1st and the 2000th cycles, clearly evidencing the excellent stability of the electrode materials. This stability of HC-VGS is superior as compared to other typical 3D nanocarbon structures reported in the literature; for example, Bai *et al.* obtained 95% retention after 2000 cycles for crystalline composites of NiO, reduced graphenes oxide, and carbon nanotubes; Zhao *et al.* obtained 94.4% retention after 2000

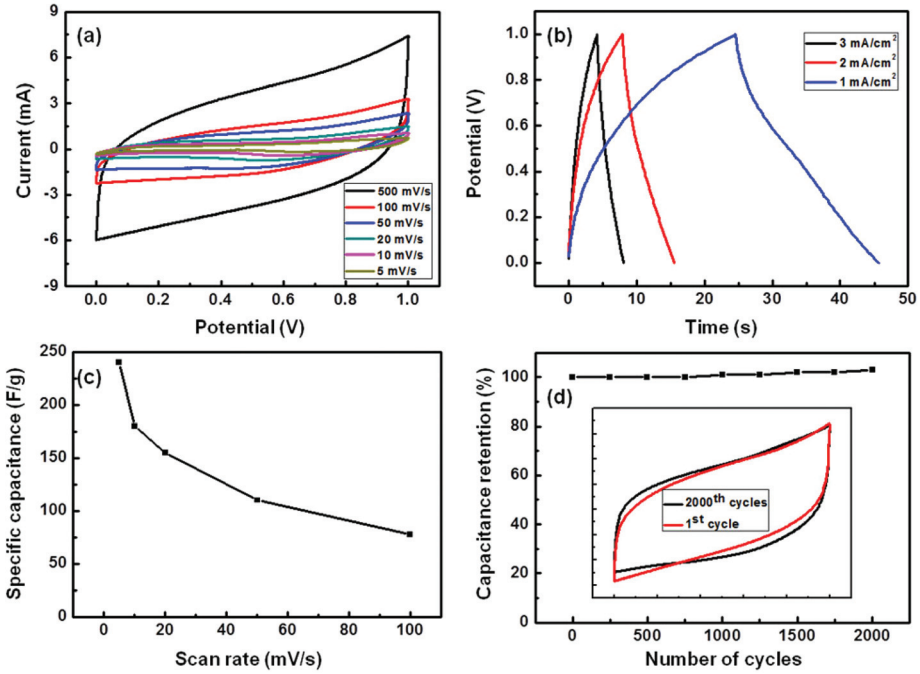

Fig. 3 Supercapacitor performance of HC-VGS. CV curves of (a) HC-VGS at different scan rates of 5, 10, 20, 50, 100 mV s^{-1} and 500 mV s^{-1}. (b) Galvanostatic charge/discharge plots of HC-VGS at current densities of 3, 2 and 1 mA cm^{-2}. (c) Rate capabilities of HC-VGS, and (d) cycle stability of HC-VGS at a scan rate of 400 mV s^{-1} for 2000 cycles.

cycles for graphene nanosheets hybridized with $Co(OH)_2$.[41,42] A slight increase in capacitance was observed at the end of 2000 cycles which could arise from an increased wetting of electrodes through capillary action in the successive cycles. We attribute such an good stability to the structural durability and the EDL charge storage mechanism of carbon-based materials, as opposed to metal oxide nanostructures which often show low capacitance retention due to a significant degradation to the nanostructures through redox reactions.[43]

The EIS spectrum for HC-VGS measured in the three-electrode configuration is shown in the Nyquist plot in Fig. S3,† where the frequency-dependent impedance is presented as the real (Z') and imaginary (Z'') components. As-grown HC-VGS displayed a vertical curve feature at low frequencies, indicating a near ideal capacitive behavior.[34] We also report a low charge transfer resistance and electrode resistance of 2 Ω and 3.7 Ω respectively, which indicates that the HC-VGS possesses a highly conductive surface. In the high-frequency range, a semicircle was observed to intersect with the real (Z') axis, which could be attributed to charge transfer at the electrode–electrolyte interface.[44] We have also performed the three-electrode cell measurements to better evaluate the potential of HC-VGS electrode materials (Fig. S4†).[45] The resulting three electrode measurement was consistent with two-electrode-based results. Our supercapacitor performance result demonstrates that HC-VGS which was derived from natural wax may be a promising material for the future energy storage devices. This advantageous characteristic may result from the highly-dense network structure and thin graphitic edges, as suggested from the morphology of HC-VGS, and may also be utilized for a good biosensing platform, which will be discussed in the next section.

Biosensing performance of HC-VGS electrodes

When considering the major life-threatening and debilitating diseases prevalent in the modern society, neurodegenerative dementias such as Alzheimer's disease (AD) present a widespread and rising incidence with far-reaching and detrimental socio-economic repercussions.[46] AD may be most effectively managed with therapeutics provided the disease is accurately diagnosed in the early stages. In order to identify and monitor the progression of AD in sufferers, the specific detection of biomarkers which hallmark the lesions associated with AD is required. One such biomarker is the aggregated form of the Aβ peptide, namely, the oligomeric Amyloid-beta (Aβ-O) which is present in the cerebrospinal fluid (CSF) of AD sufferers.[47,48] The Aβ peptide exists in the CSF as unaggregated monomers (Aβ-M) and as aggregated oligomers, whereby the former is benign, and the latter is neurotoxic. Therefore, there is a need for a sensor which can reliably differentiate between Aβ-O and Aβ-M.

Recently, curcumin has emerged as a promising candidate which selectively binds to aggregated Aβ peptides.[49] Thus, by functionalizing our as-grown HC-VGS with curcumin, a selective sensing towards the neurotoxic Aβ-O may be enabled. Fig. 4(a) illustrates the sensing principle and the fabrication process of our HC-VGS-based biosensor. In particular, with the integration of HC-VGS as a sensing platform, its thin reactive

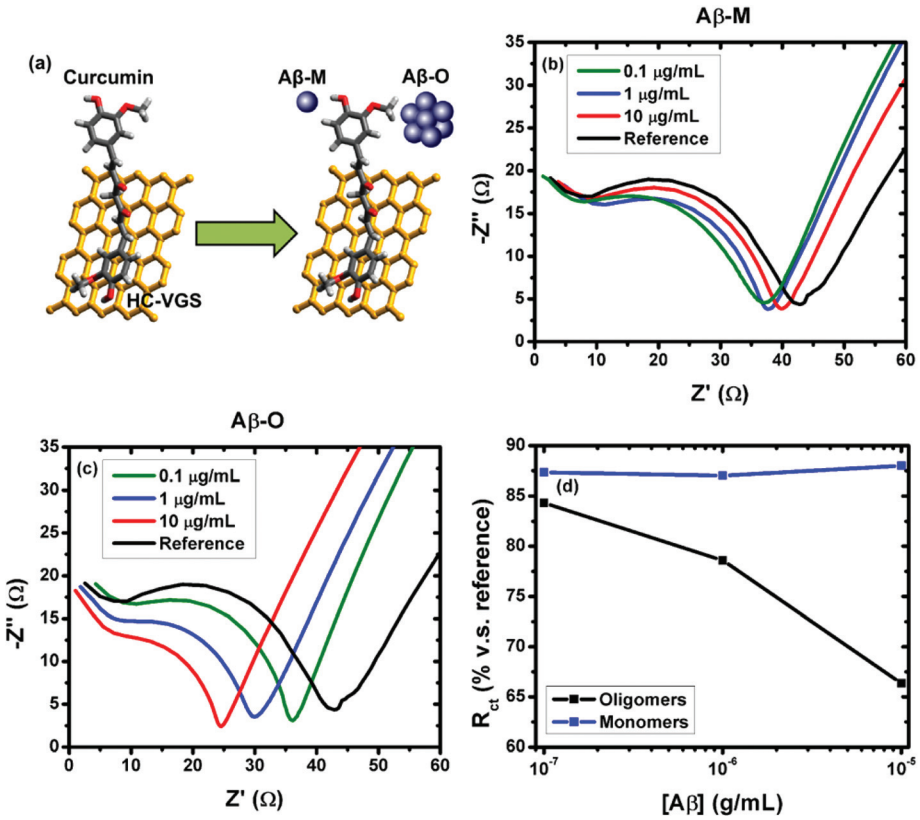

Fig. 4 Biosensing performance of curcumin-functionalized HC-VGS. (a) Schematic for the sensing protocol of Aβ-M and Aβ-O. (b) and (c), EIS response in the presence of Aβ-M, and Aβ-O, respectively, at different concentrations of 0.1, 1, and 10 μg mL^{-1}. (d) Charge transfer resistance, R_{ct}, expressed as a percentage of the blank reference, at peptide concentrations of 0.1, 1, and 10 μg mL^{-1}.

open edges and inherently large surface area enable the stable and chemical immobilization of curcumin (Fig. S5†). In addition, the high electrical conductivity of HC-VGS further enables a good sensitivity for the electrochemical detection of Aβ-O.

Fig. 4(b) shows the EIS response of our biosensor in the presence of Aβ-M at different peptide concentrations. Overall, the radius of the semicircle region shows negligible shift from the reference. This indicates there is a negligible change in the charge transfer resistance, and may also suggest a weak interaction between the Aβ-M and curcumin bioreceptors.

On the other hand, Fig. 4(c) demonstrates the EIS response in the presence of neurotoxic Aβ-O. A significant decrease in the radius of the semicircle region is evident for increasing concentrations of Aβ-O. This result may indicate that curcumin possesses a greater reactivity with the aggregated form of the Aβ peptide, namely, the reaction of curcumin with Aβ-O is more favourable than with Aβ-M. Additionally, this indicates a decrease in charge transfer resistance (R_{ct}) as more Aβ-O binds to the surface-immobilized curcumin biomolecules. Correspondingly, this decrease in R_{ct} may result from a charge injection to the HC-VGS electrode by the Aβ-Os, in particular, due to the presence of electrochemically active residues in the Aβ peptide.[50,51]

Further, Fig. 4(d) summarizes the changing trends in charge transfer resistance for the oligomeric and monomeric species at different concentrations. Unlike the case with Aβ-M, the presence of Aβ-O induces a significant decrease in the charge transfer resistance. Therefore, this result indicates that our sensor possesses a good selectivity towards Aβ peptide concentrations in the limit of 0.1 μg mL^{-1}. Moreover, we suggest that this specificity towards Aβ-O is enabled by a conformational recognition of curcumin to the secondary protein structures present in the aggregated Aβ peptide. In particular, as curcumin is symmetrical molecule composed of two polar groups separated by a hydrophobic bridge, this allows an alignment of curcumin molecules along the axis of the stacked peptide strands present in oligomers. This in turn facilitates the electrostatic interactions between the polar groups of curcumin and the positive charges on the protonated antiparallel Aβ peptides.[49]

Thus, we have demonstrated the functionality of HC-VGS as a promising and versatile base material for integration in future biosensing devices. Importantly, the favourable morphological and electrochemical properties of HC-VGS facilitate a reliable and easy-to-fabricate sensor with good sensitivity and selectivity towards the neurotoxic Aβ-O species. With future optimizations to explore the functionalization of

HC-VGS and the loading of curcumin receptors, the performace of this HC-VGS-based biosensor may be further enhanced.

Conclusions

In summary, we have demonstrated an efficient plasma-enabled reforming of the natural by-product precursor, honeycomb, into VGS with excellent morphological and electrochemical properties. Furthermore, these unique and intrinsic properties of HC-VGS enabled its excellent integration as a base material for energy storage and biosensing applications. In particular, we have assembled a reliable, simple-to-fabricate, and inexpensive biosensor which capitalized on the unique properties of HC-VGS, to enable a firm surface-immobilization of curcumin, and its novel function as a bioreceptor for a selective and sensitive capture of the neurotoxic Aβ biomarkers of AD. In addition, we have demonstrated a binder-free supercapacitor electrode, which exhibited a high specific capacitance up to 240 F g^{-1} at a scan rate of 5 mV s^{-1} and 100% capacitance retention after 2000 cycles at a high scan rate.

Importantly, these results are promising for future sustainable management of resources, through the reforming of natural by-products into carbon-based electrodes, and may also lead to better understanding of the elementary charge storage and transfer processes, which remain critical for developments in the next-generation of energy storage and biomedical devices.

Acknowledgements

This work is supported by the Australian Research Council (ARC) and CSIRO's OCE Science Leader Program. DHS acknowledges the Australian Postgraduate Award (APA) and CSIRO's OCE Postdoctoral Fellowship Program. SP acknowledges the APA and the CSIRO's OCE top-up scholarship. SY acknowledges the University of Sydney's Postgraduate Award (UPA). ZJH and KO acknowledge the support from the DECRA and Future Fellowships from the ARC, respectively.

Notes and references

1 A. J. Hunt, T. J. Farmer and J. H. Clark, in *Element Recovery and Sustainability*, The Royal Society of Chemistry, 2013, pp. 1–28, DOI: 10.1039/9781849737340-00001.
2 D. H. Seo, A. E. Rider, S. Kumar, L. K. Randeniya and K. Ostrikov, *Carbon*, 2013, **60**, 221.
3 M. Biswal, A. Banerjee, M. S. Deo and S. Ogale, *Energy Environ. Sci.*, 2013, **6**, 1249–1259.
4 S. Unarunotai, Y. Murata, C. E. Chialvo, N. Mason, I. Petrov, R. G. Nuzzo, J. S. Moore and J. A. Rogers, *Adv. Mater.*, 2010, **22**, 1072.
5 A. K. Geim and K. S. Novoselov, *Nat. Mater.*, 2007, **6**, 183–191.
6 Z. Chen, W. Ren, L. Gao, B. Liu, S. Pei and H.-M. Cheng, *Nat. Mater.*, 2011, **10**, 425.
7 A. H. Castro Neto, F. Guinea, N. M. R. Peres, K. S. Novoselov and A. K. Geim, *Rev. Mod. Phys.*, 2009, **81**, 109.
8 J. R. Miller, R. A. Outlaw and B. C. Holloway, *Science*, 2010, **329**, 1637–1639.
9 D. H. Seo, S. Kumar and K. Ostrikov, *J. Mater. Chem.*, 2011, **21**, 16339.
10 N. G. Shang, P. Papakonstantinou, M. McMullan, M. Chu, A. Stamboulis, A. Potenza, S. S. Dhesi and H. Marchetto, *Adv. Funct. Mater.*, 2008, **18**, 3506.
11 K. Ostrikov, *Rev. Mod. Phys.*, 2005, **77**, 489–511.
12 T. Kato and R. Hatakeyama, *Nat. Nanotechnol.*, 2012, **7**, 651.
13 K. Ostrikov, E. C. Neyts and M. Meyyappan, *Adv. Phys.*, 2013, **62**, 113–224.
14 D. H. Seo, Z. J. Han, S. Kumar and K. Ostrikov, *Adv. Energy Mater.*, 2013, **3**, 1316–1323.
15 Z. Bo, Y. Yang, J. Chen, K. Yu, J. Yan and K. Cen, *Nanoscale*, 2013, **5**, 5180–5204.
16 K. L. Youmans, L. M. Tai, T. Kanekiyo, W. B. Stine, S. C. Michon, E. Nwabuisi-Heath, A. M. Manelli, Y. F. Fu, S. Riordan, W. A. Eimer, L. Binder, G. J. Bu, C. J. Yu, D. M. Hartley and M. J. LaDu, *Mol. Neurodegener.*, 2012, **7**, 8.
17 H. Nishide and K. Oyaizu, *Science*, 2008, **319**, 737–738.
18 S. Yick, Z. J. Han and K. Ostrikov, *Chem. Commun.*, 2013, **49**, 2861–2863.
19 M. F. El-Kady, V. Strong, S. Dubin and R. B. Kaner, *Science*, 2012, **335**, 1326–1330.
20 A. E. Rider, S. Kumar, S. A. Furman and K. Ostrikov, *Chem. Commun.*, 2012, **48**, 2659.
21 P. Lespade, R. Al-Jishi and M. S. Dresselhaus, *Carbon*, 1982, **20**, 427.
22 Y. Wang, D. C. Alsmeyer and R. L. McCreery, *Chem. Mater.*, 1990, **2**, 557.
23 A. Cuesta, P. Dhamelincourt, J. Laureyns, A. Martinez-Alonso and J. M. D. Tascon, *J. Mater. Chem.*, 1998, **8**, 2875.
24 S. Niyogi, E. Bekyarova, M. E. Itkis, H. Zhang, K. Shepperd, J. Hicks, M. Sprinkle, C. Berger, C. N. Lau, W. A. de Heer, E. H. Conrad and R. C. Haddon, *Nano Lett.*, 2011, **10**, 4061.
25 G. Ruan, Z. Sun, Z. Peng and J. M. Tour, *ACS Nano*, 2011, **5**, 7601.
26 Z. Yang, J. Zhang, M. C. W. Kintner-Meyer, X. Lu, D. Choi, J. P. Lemmon and J. Liu, *Chem. Rev.*, 2011, **111**, 3577–3613.
27 J. Tollefson, *Nature*, 2011, **473**, 134–135.
28 R. F. Service, *Science*, 2006, **313**, 902.
29 A. Manthiram, Y. Fu and Y.-S. Su, *J. Phys. Chem. Lett.*, 2013, **4**, 1295–1297.
30 J. R. Miller and P. Simon, *Science*, 2008, **321**, 651–652.
31 H. Jiang, P. S. Lee and C. Li, *Energy Environ. Sci.*, 2013, **6**, 41–53.
32 X. Zhang, H. Zhang, C. Li, K. Wang, X. Sun and Y. Ma, *RSC Adv.*, 2014, **4**, 45862–45884.

33 F. Wang, S. Xiao, Y. Hou, C. Hu, L. Liu and Y. Wu, *RSC Adv.*, 2013, **3**, 13059–13084.
34 P. L. Taberna, P. Simon and J. F. Fauvarque, *J. Electrochem. Soc.*, 2003, **150**, A292–A300.
35 P. Simon and Y. Gogotsi, *Acc. Chem. Res.*, 2013, **46**, 1094–1103.
36 J. Yan, J. Liu, Z. Fan, T. Wei and L. Zhang, *Carbon*, 2012, **50**, 2179–2188.
37 L. Qie, W. Chen, H. Xu, X. Xiong, Y. Jiang, F. Zou, X. Hu, Y. Xin, Z. Zhang and Y. Huang, *Energy Environ. Sci.*, 2013, **6**, 2497.
38 Z. Yan, L. Ma, Y. Zhu, I. Lahiri, M. G. Hahm, Z. Liu, S. Yang, C. Xiang, W. Lu, Z. Peng, Z. Sun, C. Kittrell, J. Lou, W. Choi, P. M. Ajayan and J. M. Tour, *ACS Nano*, 2013, **7**, 58–64.
39 L. Zhang, F. Zhang, X. Yang, G. Long, Y. Wu, T. Zhang, K. Leng, Y. Huang, Y. Ma, A. Yu and Y. Chen, *Sci. Rep.*, 2013, **3**, 1408.
40 J. H. Lee, N. Park, B. G. Kim, D. S. Jung, K. Im, J. Hur and J. W. Choi, *ACS Nano*, 2013, **7**, 9366–9374.
41 Y. Bai, M. Du, J. Chang, J. Sun and L. Gao, *J. Mater. Chem. A*, 2014, **2**, 3834–3840.
42 C. Zhao, W. Zheng, X. Wang, H. Zhang, X. Cui and H. Wang, *Sci. Rep.*, 2013, **3**, 2986.
43 B. E. Conway, V. Birss and J. Wojtowicz, *J. Power Sources*, 1997, **66**, 1–14.
44 D. Aurbach, M. D. Levi, E. Levi, H. Telier, B. Markovsky, G. Salitra, U. Heider and L. Hekier, *J. Electrochem. Soc.*, 1998, **145**, 3024–3034.
45 M. D. Stoller and R. S. Ruoff, *Energy Environ. Sci.*, 2010, **3**, 1294–1301.
46 A. Abbott, *Nature*, 2011, **475**, S2–S4.
47 K. Blennow, H. Hampel, M. Weiner and H. Zetterberg, *Nat. Rev. Neurol.*, 2010, **6**, 131–144.
48 H. W. Querfurth and F. M. LaFerla, *N. Engl. J. Med.*, 2010, **362**, 329–344.
49 F. Yang, G. P. Lim, A. N. Begum, O. J. Ubeda, M. R. Simmons, S. S. Ambegaokar, P. P. Chen, R. Kayed, C. G. Glabe, S. A. Frautschy and G. M. Cole, *J. Biol. Chem.*, 2005, **280**, 5892–5901.
50 M. Vestergaard, K. Kerman, M. Saito, N. Nagatani, Y. Takamura and E. Tamiya, *J. Am. Chem. Soc.*, 2005, **127**, 11892–11893.
51 P. Lopes, M. Xu, M. Zhang, T. Zhou, Y. Yang, C. Wang and E. E. Ferapontova, *Nanoscale*, 2014, **6**, 7853–7857.